Applied Nanoscience

Cu-doped C3N4-MgO nanorods for bactericidal and dye degradation performance

--Manuscript Draft--

Manuscript Number:	APNA-D-21-01666
Full Title:	Cu-doped C3N4-MgO nanorods for bactericidal and dye degradation performance
Article Type:	Original Article
Abstract:	Photocatalytic and magnetic stability of two-dimensional layered nanomaterials is improved by metal doping, which is a potential eco-friendly technique widely used in various industrial sectors. In this study, economical and convenient co-precipitation method was adopted to synthesize copper (Cu) doped in various concentrations (2.5, 5, 7.5 and 10%) into fixed amount of C_3N_4/MgO nanostructures for efficient photocatalytic and bactericidal activities. Improved crystallinity and increase in crystal size upon doping was confirmed with XRD analysis, which was corroborated with SAED results. FTIR spectroscopy revealed that MgO spectra consisted of stretching vibrations of Mg-O bond and other functional groups with minor changes in the vibrational modes upon doping. A HR-TEM fitted with Gatan® digital software indicated the formation of hexagonal phase in as-prepared sample and nanorods upon doping, with confirmed d-spacing values. The UV-Vis analysis revealed a slight redshift in absorption intensity leading to decreased band gap (Eg) for Cu-doped MgO/C_3N_4. Photoluminescence (PL) spectra were acquired to investigate the recombination of electron-hole pairs. To evaluate the elemental and surface composition with binding energy alterations of Cu-doped C_3N_4-MgO nanorods, XPS was employed. Thermal stability and behavior of synthesized samples was investigated by DSC thermoanalytical analysis. Photocatalytic performances of as-prepared samples were evaluated against methylene blue ciprofloxacin (MBCF) dye in acidic, neutral and basic medium. Furthermore, efficient antibacterial potential was evaluated against Escherichia Coli (*E. coli*) and Staphylococcus aureus (*S. aureus*) bacteria.

Cu-doped C_3N_4-MgO nanorods for bactericidal and dye degradation performance

M. U. Akbar[a], M. Ikram[a*], M. Imran[b], A. Haider[c], A. Ul-Hamid[d]*, S. Dilpazir[e], A. Shahzadi[f], W. Nabgan[g*], J. Haider[h]

[a]Solar Cell Applications Research Lab, Department of Physics, Government College University, Lahore, 54000, Punjab, Pakistan

[b]State Key Laboratory of Chemical Resource Engineering, Beijing Advanced Innovation Centre for Soft Matter Science and Engineering, Beijing Engineering Center for Hierarchical Catalysts, Beijing University of Chemical Technology, Beijing 100029, China

[c]Department of Clinical Medicine and Surgery, University of Veterinary and Animal Sciences, Lahore 54000, Punjab, Pakistan

[d]Core Research Facilities, King Fahd University of Petroleum & Minerals, Dhahran, 31261, Saudi Arabia

[e]CAS Key Laboratory of Green Process and Engineering, Institute of Process Engineering, Chinese Academy of Sciences, Beijing, P. R. China

[f]Punjab University College of Pharmacy, University of the Punjab, 54000, Lahore, Pakistan

[g]School of Chemical and Energy Engineering, Faculty of Engineering, Universiti Teknologi Malaysia, 81310 Skudai, Johor, Malaysia.

[h]Tianjin Institute of Industrial Biotechnology, Chinese Academy of Sciences, Tianjin 300308, China

*Corresponding authors emails: [a]dr.muhammadikram@gcu.edu.pk, [c]anwar@kfupm.edu.sa, [g]wnabgan@gmail.com

ABSTRACT

Photocatalytic and magnetic stability of two-dimensional layered nanomaterials is improved by metal doping, which is a potential eco-friendly technique widely used in various industrial sectors. In this study, economical and convenient co-precipitation method was adopted to synthesize copper (Cu) doped in various concentrations (2.5, 5, 7.5 and 10%) into fixed amount of C_3N_4/MgO nanostructures for efficient photocatalytic and bactericidal activities. Improved crystallinity and increase in crystal size upon doping was confirmed with XRD analysis, which was corroborated with SAED results. FTIR spectroscopy revealed that MgO spectra consisted of stretching vibrations of Mg-O bond and other functional groups with minor changes in the vibrational modes upon doping. A HR-TEM fitted with Gatan® digital software indicated the formation of hexagonal phase in as-prepared sample and nanorods upon doping, with confirmed d-spacing values. The UV-Vis analysis revealed a slight redshift in absorption intensity leading to decreased band gap (Eg) for Cu-doped MgO/C_3N_4. Photoluminescence (PL) spectra were acquired to investigate the recombination of electron-hole pairs. To evaluate the elemental and surface composition with binding energy alterations of Cu-doped C_3N_4-MgO nanorods, XPS was employed. Thermal stability and behavior of synthesized samples was investigated by DSC thermoanalytical analysis. Photocatalytic performances of as-prepared samples were evaluated against methylene blue ciprofloxacin (MBCF) dye in acidic, neutral and basic medium. Furthermore, efficient antibacterial potential was evaluated against Escherichia Coli (*E. coli*) and Staphylococcus aureus (*S. aureus*) bacteria.

Keywords: Co-precipitation, C_3N_4, nanorods; MgO; Antimicrobial; XPS; DSC-TGA

1. INTRODUCTION

Nanotechnology has evolved into a fascinating discipline in the current period, with several applications in biology, health, energy, and materials science, among others [1–5]. Approximately, 5-10 billion dollars per year are being spent on clinical complications associated with infected implanted medical devices that prolong hospital stays and cause medical complications for patients [6]. Typical antibiotics used to treat nosocomial infections are not able to penetrate biofilms, which results in making bacteria and fungi more drug resistant and hard to eliminate. [7, 8]. Therefore, biomaterials are crucial to eliminate microbial infections and linkage, reducing antibiotics use and extenuating infections of medical devices [9].

Many metal oxide nanoparticles (NPs) have been used for this purpose as they have shown considerable antimicrobial properties. Metal-oxide NPs are extremely fascinating due to their remarkable applications in the electronics fields, catalysis, sensing, and so forth [10–19]. Fabrication of metal oxide NPs with different morphologies is becoming prominent due to their significant properties [20, 21]. High surface-to-volume ratio of one-dimensional nanostructures including wires, fibers and rods make them highly attractive for various applications [22]. From among all metal oxides, MgO (magnesium oxide) is a potential oxide that can be prepared easily in versatile structural forms and different sizes [23]. MgO has found many applications in the field of photocatalysis, bio-compatibility and antibacterial activities. MgO NPs have been used as substantial material in bioremediation, additives in refractories, superconducting products, water treatments, paints and specially in medicines for the relief of heartburn, sore stomach, acid digestive disorders and for bone regeneration [24–26]. This is due to the wide energy band gap E_g, thermochemical stability and impressive surface reactivity of MgO NPs [27]. Various precursors have been utilized for MgO preparation using different methods co-precipitation, solgel, combustion, hydrothermal and spray pyrolysis [13, 28, 29]. Different crystal structures can be obtained from metal elements of different oxides which can be insulators, semiconductors and metallic, that are very useful in chemical reactivity [30]. In principle, behavior of metal containing molecules in different oxides depend on electrostatic force produced by charges and mixing of orbitals of molecules with conduction and valance bands (CB and VB respectively), and dipole of molecules [31].

Due to physiochemical nature of metal-containing elements exhibiting some interesting properties such as large E_g, chemical inertness, thermal stability and high dielectric constant, MgO has become one of the most important materials in industry today [32, 33]. MgO as a bulk material have a very large E_g which reduces its application as a semiconductor [34]. Doping of metals in metal oxides tend to decrease E_g of materials normally making them conductors and advances its applications in electronics. Cu is a very interesting metal as it contains negatively charged electron in its complete orbital near positive charged nucleus. Application of Cu is very fascinating in antibacterial activity, as very low amount of Cu induces inactivation of bacteria in dark [35]. This enhanced antibacterial effect is mainly attributed to Cu ions, surface contact killing and Cu obtaining reactive oxygen species (ROS) in O_2 presence. This bacterial inactivation by Cu has been recorded to take place in both anaerobic and aerobic conditions [36]. Graphitic carbon nitride (C_3N_4) is also an interesting compound for its application in photocatalysis and antimicrobial activities. In several carbon compounds, C_3N_4 surface offers electron rich qualities and multiple modified functionalities. Water decomposition by C_3N_4 is a milestone when it comes to its application in photocatalysis. This is ascribed to the fact that this novel material does not contain metal and metallic elements and causes unnecessary damage and environmental toxicity [37]. Aim of this study is to prepare Cu-doped C_3N_4/MgO nanostructures with various Cu concentrations, via co-precipitation method and to check its antimicrobial and photocatalytic properties.

2. EXPERIMENTAL DETAILS

2.1 Materials

Magnesium chloride ($MgCl_2.6H_2O$, 99-102%), copper chloride ($CuCl_2.2H_2O$, 99%) and urea (CH_4N_2O) were obtained from Sigma Aldrich, Germany. Carbon nitride (g-C_3N_4) was obtained via pyrolysis of urea (CH_4N_2O). Without further purification, all chemicals have been utilised.

2.2 Synthesis of MgO and Cu-C_3N_4/MgO

Controlled material (MgO) was prepared in laboratory. Briefly, $MgCl_2.6H_2O$ (4g) was dissolved in 100 mL of deionized (DI) water and the mixture was allowed to react for 15 min under constant stirring. One molar solution was prepared in 100 ml of water with 4g of ($MgCl_2$. $6H_2O$) and 100 mg of (C_3N_4) was added in solution (Fig. 1). Firstly, solution of ($MgCl_2$. $6H_2O$) and (C_3N_4) was prepared and then different concentrations (2.5%, 5%, 7.5% and 10%) of ($CuCl_2.2H_2O$) were doped into solution of C_3N_4/MgO. Firstly, prepared solution was put on hot plate at 200^o C for three hours under constant stirring. Following this, sample was sonicated for half an hour with ultrasonic rays followed by centrifugation at 7500 rpm for ten min. Lastly, samples were annealed at 450^o C for two hours.

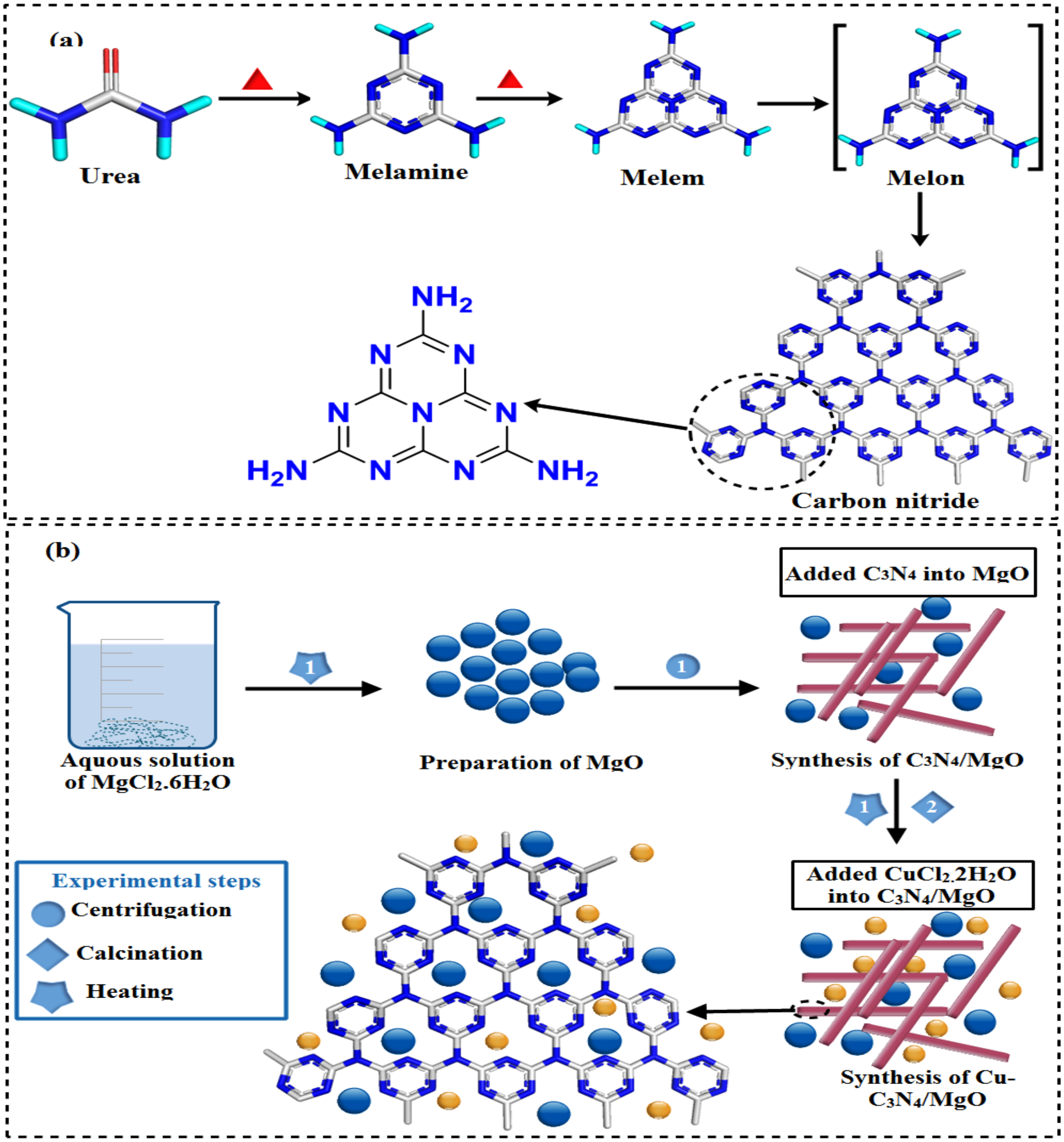

Figure. 1 (a) Formation mechanism of carbon nitride obtained from urea pyrolysis. **(b)** Schematic illustration of fabrication of Cu-C_3N_4/MgO samples.

3. RESULTS AND DISCUSSION

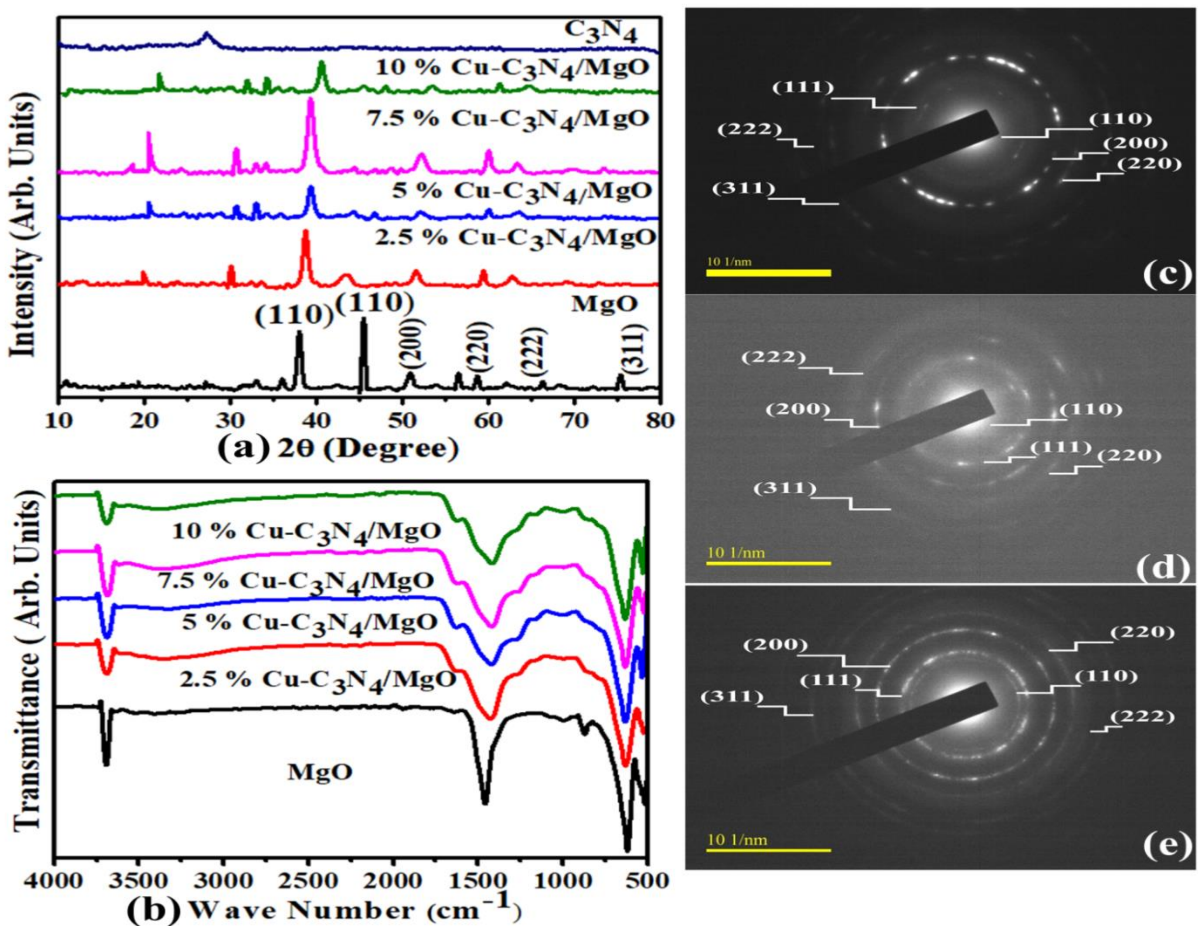

Figure 2. (a) XRD spectra (b) FTIR spectra and SAED patterns of MgO (c), 7.5% Cu-C_3N_4/MgO (d) and 10% Cu-C_3N_4/MgO (e).

Structural and phase properties of prepared samples were examined through x-ray diffraction in $2\theta^o$ range 8^o -80^o as depicted in Fig. 2 (a). Peaks generated at 38.01^o, 45.03^o, 50.87^o, 58.67^o, 66.17^o and 76.53^o indexed to (110), (111), (200), (222), (220), and (311) planes, respectively belonged to FCC cubic structure of MgO (JCPDS Card No. 87-0653). C_3N_4 peaks were not detected in doped samples due to their lower concentration relative to MgO. The impact of dopants Cu and C_3N_4 were found in peaks shift toward higher $2\theta^o$ values. Upon doping, peak broadening was observed which led to decrement in crystalline size and showed successful incorporation of dopants into the matrix [38]. Peaks (200), (220) and (311) contracted for doped samples might indicate distortion of typical FCC crystalline structure at least in some specific directions identifying rod-like structure of prepared samples. Additional peaks observed at 33.03^o, 51.09^o and 56.87 in spectra depicted the presence of hydroxyl group $Mg(OH)_2$ [39]. Fig 2(c-e) shows SAED (Selected Area Electron Diffraction) patterns for MgO,7.5% and 10% Cu-doped C_3N_4-MgO indexed with planes (110), (111), (200), (220), (222) and (311) of MgO that were compatible with XRD results. To analyze chemical composition and the presence of various functional groups in samples, FTIR spectroscopy was performed (Fig. 2b). The broad band range (3040–3550 cm^{-1}) indicated MgO nanostructures formation while broad band in 620-873 cm^{-1} range was ascribed to vibrations of Mg-O bond [25, 40]. The distinct bands observed at 880 and 1410 cm^{-1} represent vibrations of surface hydroxyl group (1). Sharp peak at 3695 cm^{-1} is accredited to stretching of O–H bond.

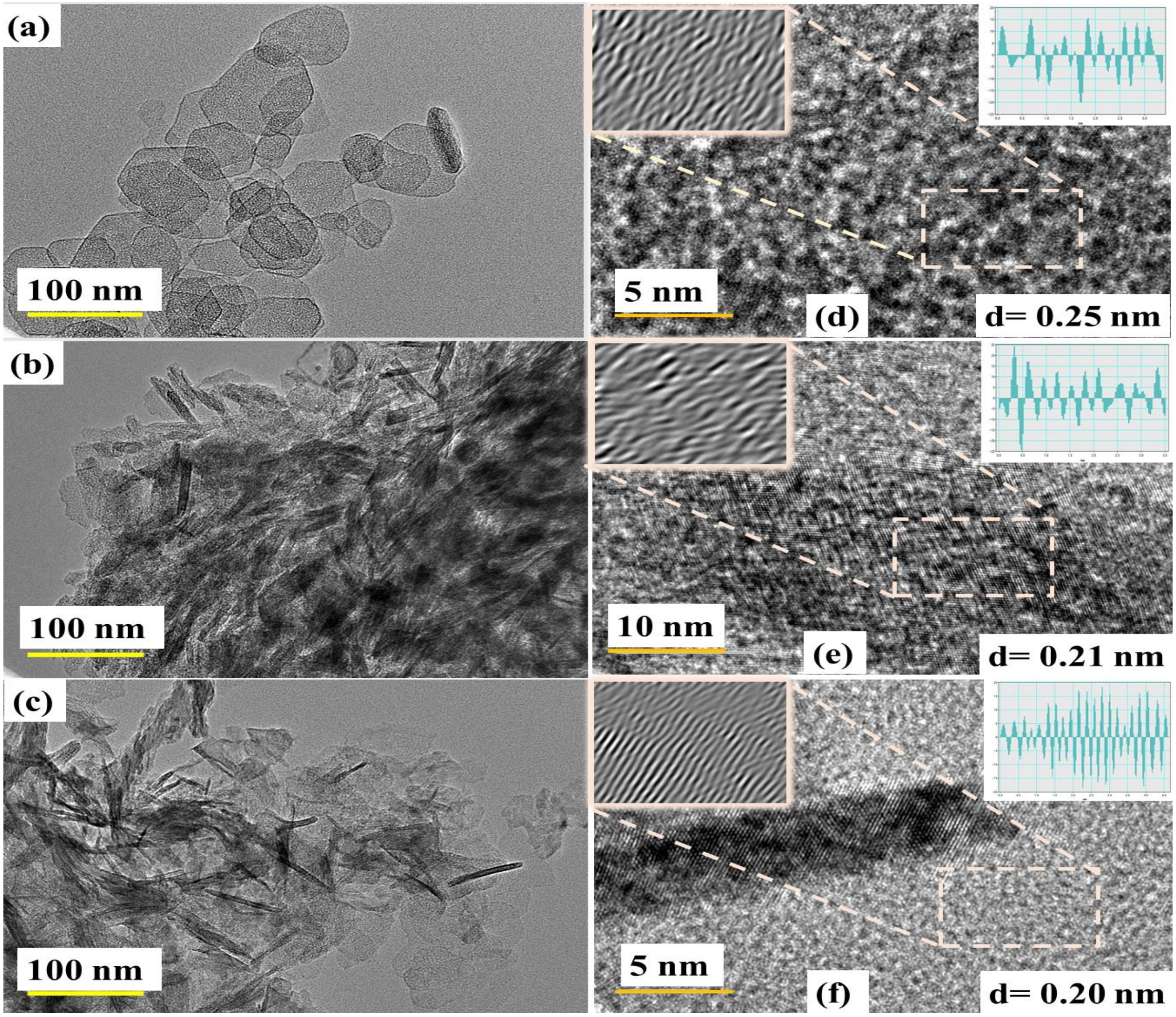

Figure 3: (a) MgO (b) 7.5% and (c) 10% Cu-C_3N_4/MgO illustrated HRTEM images and lattice fringes of MgO, 7.5% Cu-C_3N_4/MgO and 10% Cu-C_3N_4/MgO are represented in (d), (e) and (f), respectively.

HRTEM was employed to study the morphology and surface topology of prepared samples. Image of 100 nm size for MgO exhibited cubic structure formation due to the aggregation of several thousand NPs (Fig. 3a). 7.5% and 10% Cu-doped C_3N_4/MgO depicted dense and interconnected nanorods such that no clear boundary existed between them, see (Fig. 3b) and (Fig. 3c) respectively. Lattice fringes were separated by distance of 0.25 nm, 0.21 nm and 0.20

nm for MgO, 7.5% Cu-C_3N_4/MgO and 10% Cu- C_3N_4/MgO, respectively (Fig. 3(c-e)). HRTEM and d-spacing of 2.5 and 5% samples are shown in Fig. S1.

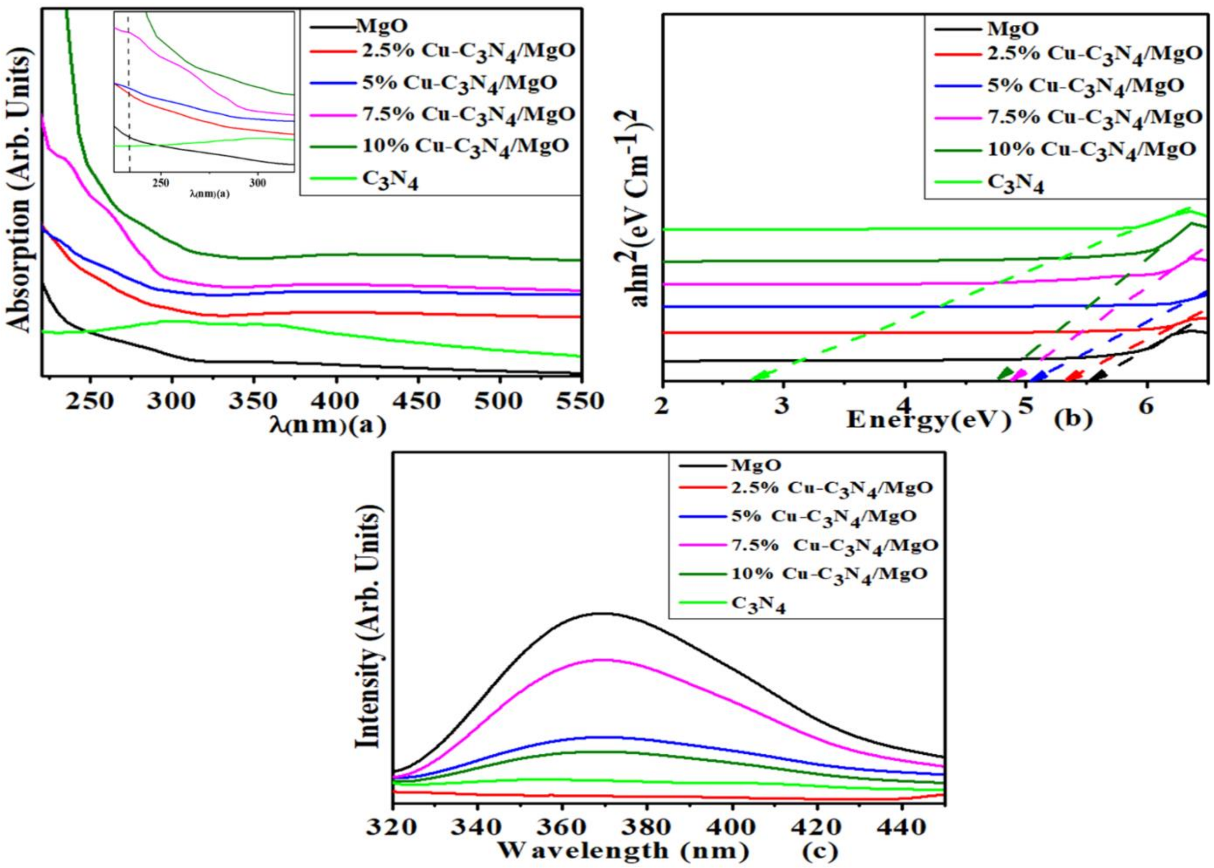

Figure 4: (a) Band gap (b) UV-Vis Spectra (c) PL spectra of prepared samples.

The optical absorption spectra of MgO- and Cu-doped C_3N_4/MgO were recorded to investigate typical properties in UV-Vis region (Fig. 4a). MgO showed absorption in the region 230-310 nm and redshift was observed upon increasing concentration of Cu in C_3N_4/MgO composites. This absorption is significantly greater than bulk MgO because of bulk excitonic transitions. This is due to the electrostatic potential of O_2 in MgO which slowly decreases with coordination and the whole process requires lesser energy [41]. Quantum confinement upon impurity incorporation is dependent on host crystal size, as crystal size decreases confinement degree and its effect increases [38]. The optical E_g of obtained samples were calculated from the Tauc's relation as represented in Fig. 4b. Eg for MgO was calculated to be 5.5 eV and it decreased down to 4.7 eV for Cu-doped C_3N_4/MgO. This decrease in Eg is ascribed to smaller crystallite size and agglomeration of particles to form nanorods upon doping [32].

When light falls on the surface of a material, generation of electron-hole pairs and their recombination lead to PL phenomenon. PL spectra for prepared samples are shown in Fig. 4c. Emission spectra depicted one dominant peak at 370 nm, with excitation wavelength 280 nm irradiated onto the samples. MgO being an insulator (E_g~ 5.7 eV) showed luminescence in the above-mentioned range, which is extensively ascribed to surface defects and vacancy sites excitations [42]. Photo-excitation of electrons into CB of attached oxygen atoms at step-edge defects of MgO causes luminescence [43]. Spectra recorded for Cu-doped C_3N_4/MgO composite showed significant decrease in PL intensity which may be attributed to increased amount of surface and structural defects generated after incorporation of Cu atoms in the matrix. This dramatic increase in defects act as trap sites for electrons, rendering their motion toward holes thus reducing recombination rate of excitons.

Differential scanning calorimetry (DSC) was utilized to measure the flow of heat into or out of the samples (MgO, 5% Cu-C_3N_4/MgO and 10% Cu-C_3N_4/MgO) as a function of temperature and heat flow. The DSC curves exhibited a distinctive endothermic peak at 144 $^{\circ}$C for pure MgO and this peak started to shift forward upon Cu and C_3N_4 doping into the matrix, as presented in Fig.5. For 5% Cu-C_3N_4/MgO, data showed an endothermic peak at 154 $^{\circ}$C and for 10% Cu-C_3N_4/MgO the endothermic peak is at 185 $^{\circ}$C. This shift of endothermic temperature region towards higher temperature range might be attributed to the increasing concentration of Cu in C_3N_4/MgO sample, as Cu exhibits an endothermic peak at a higher temperature region (300-450 °C) [44]. These distinctive peaks indicate the purity and thermal stability of the prepared samples [45–47].

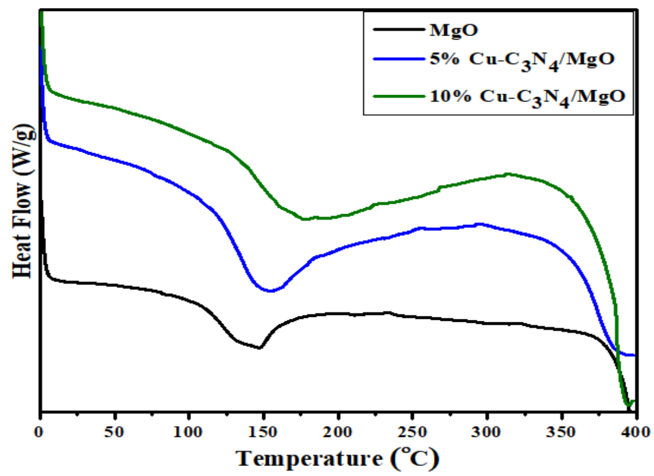

Figure 5. DSC spectra of MgO, 5% Cu-C_3N_4/MgO and 10% Cu-C_3N_4/MgO.

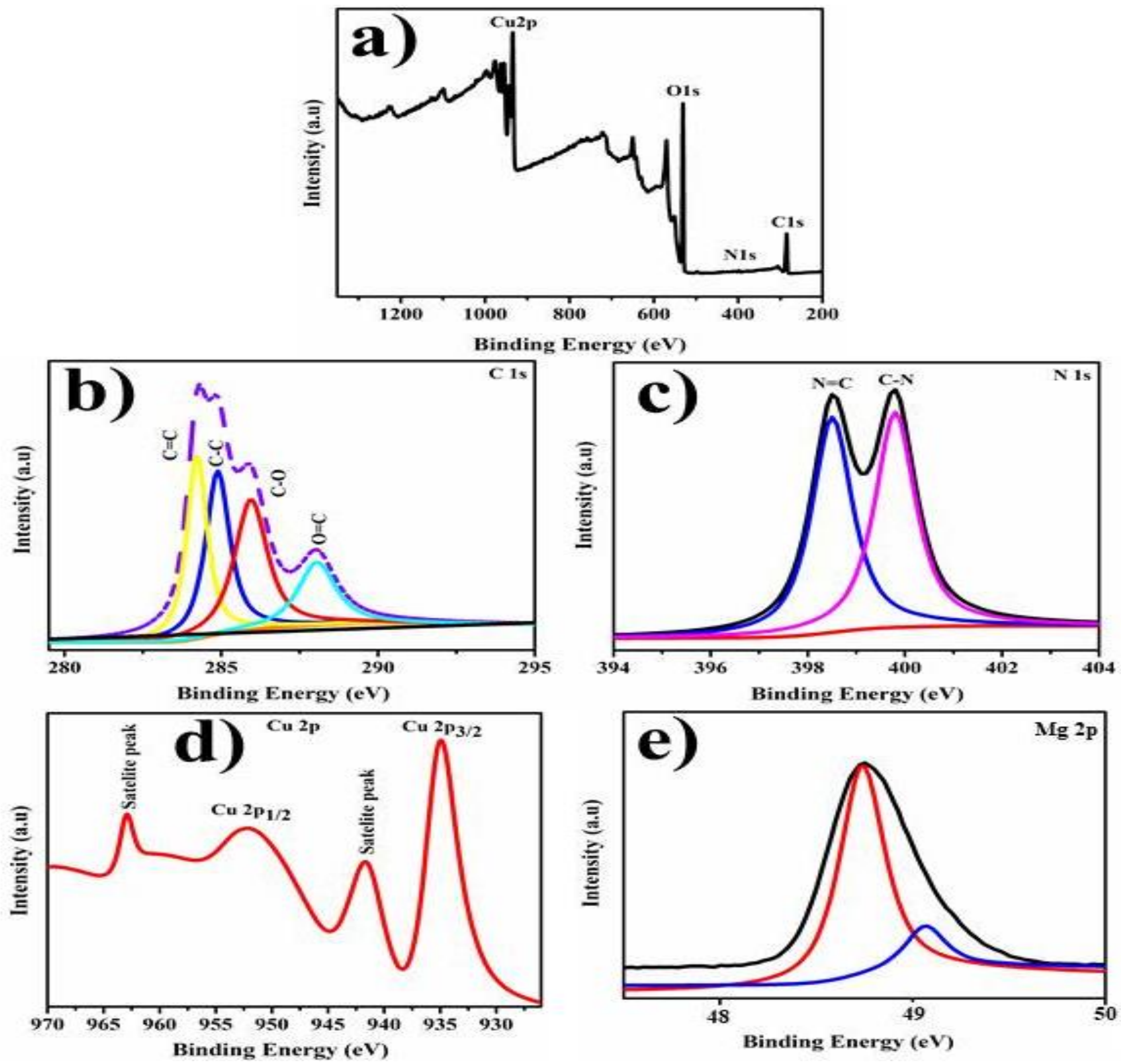

Figure 6: XPS spectra of Cu-doped C_3N_4/MgO samples.

The elemental composition, surface composition, and binding energy alterations of Cu-doped C_3N_4-MgO nanorods were determined using XPS. The survey, O 1s, N 1s, and Cu 2p high resolution spectra are shown in Fig. 6(a–e). The XPS survey spectrum displays the predicted strong signals of C, N, O, and Cu, as seen in Fig. 6 (a). The C1s peaks of the doped nanorods may be resolved into three peaks at 284.8, 286.4, and 288.4 eV, referring to the functional groups C-C/C=C, C-O, and C=O, accordingly as depicted in Fig. 6b [48]. Moreover, the N1s signal band in Fig. 6 (c) may be attributed to the N=C and C-N groups due to its binding energy of around 398.5 and 399.8 eV [49]. Notably, Fig. 6 d defined the Cu 2p pattern of doped CuO with heights at 933.3 and 953.3 eV binding energies, which correspond to the Cu $2p_{3/2}$ and Cu $2p_{1/2}$ spin orbits, accordingly, confirming the samples' divalent oxidation state. The last two peaks, at 942.2 and 962 eV, relate to the satellite heights of Cu $2p_{3/2}$ and Cu $2p_{1/2}$, which emerged principally owing to the partially filled 3d9 orbital in divalent oxidation state [50]. A high-resolution analysis of the Mg 2p core level spectrum reveals two distinct electronic states ($2p_{1/2}$, $2p_{3/2}$) with binding energies of 48.95 eV and 49.29 eV, respectively. The location of the $2p_{3/2}$, $2p_{1/2}$ peaks and the difference in their binding energies indicate the presence of Mg ions in the + 2 oxidation state as shown in Fig. 6 (e) [51].

Table 1: Bactericidal action of MgO and Cu-doped C_3N_4/MgO

	0.5mg/50µl					1.0mg/50µl				
Pathogen	[1]	[2]	[3]	[4]	[5]	[1]	[2]	[3]	[4]	[5]
S. aureus	1.55	2.65	3.45	3.95	4.05	2.05	4.4	5.35	6.45	7.05
E. coli	1.45	2.6	3.3	3.65	3.95	1.8	3.15	3.4	3.85	5.15

[1] MgO

[2] 2.5% Cu-C_3N_4/MgO

[3] 5 % Cu-C_3N_4/MgO

[4] 7.5% Cu-C_3N_4/MgO

[5] 10% Cu-C_3N_4/MgO

Fig. S2 shows the photo-degradation of methylene blue ciprofloxacin (MBCF) dye over MgO and Cu-C_3N_4/MgO nanorods as catalyst. The dye degradation in photocatalytic procedure is caused by generation of electron-hole (e^--h^+) pairs in VB and CB. Produced h^+ in VB reacts with surrounding water molecules to form OH• radicals and e^- in the CB is captured by the oxygen to generate anionic superoxide radical (O_2-•) as illustrated in Fig. 7 and explained in following equations [52]:

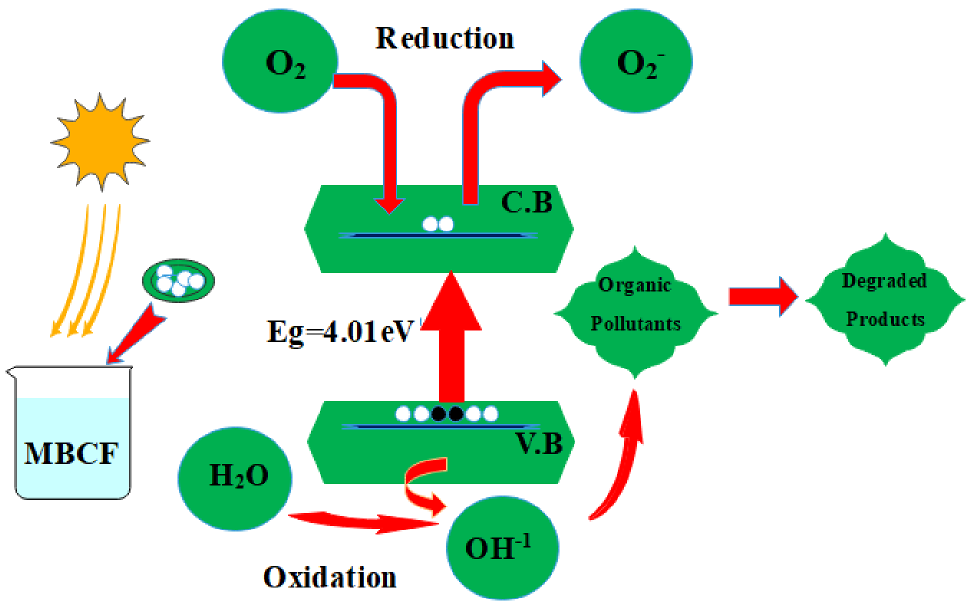

Figure 7. Illustrates photocatalytic mechanism of Cu-C_3N_4/MgO samples.

Sample + hυ → Sample (e^- + h^+) ------ (1)

$H_2O + h^+ \rightarrow \bullet OH + H^+$ -------------------(2)

The generated •OH radical are remarkably strong oxidizing agents. Molecules adsorbed or near to the surface of the catalyst are non-selectively attacked by •OH radical species which result in degradation or mineralization based on structure and stability level. The electrons in the VB interacts with oxygen molecules to generate $O_2^{-\bullet}$ species as shown in equation 3,

$O_2 + e^- \rightarrow O_2^{-\bullet}$ --------------------------- (3)

This produced superoxide gets protonated and form a hydroperoxyl radical (HO_2•) and further dissociates into highly reactive hydroxyl radicals (OH•) as presented in below equations,

$O_2^{-\bullet} + H^+ \rightarrow HOO\bullet$ ---------------------- (4)

$2HOO\bullet \rightarrow H_2O_2 + O_2$ ------------------- (5)

$\bullet OH + dye \rightarrow$ degraded products ----- (6)

The E_g of MgO is 7.8 eV normally, but for MgO nanostructures this is decreased to 5.5 eV which makes it a potential material for photo-catalysis [53, 54].

Percentage degradation of individual material is calculated using equation 7 as shown in Fig. 8 [40]:

$\% \, Degradation = \left(\frac{(Co-Ct)}{Co}\right) * 100$ ------ (7)

Here C_o and C_t are the initial and final concentration of dye after exposure to UV-Vis light.

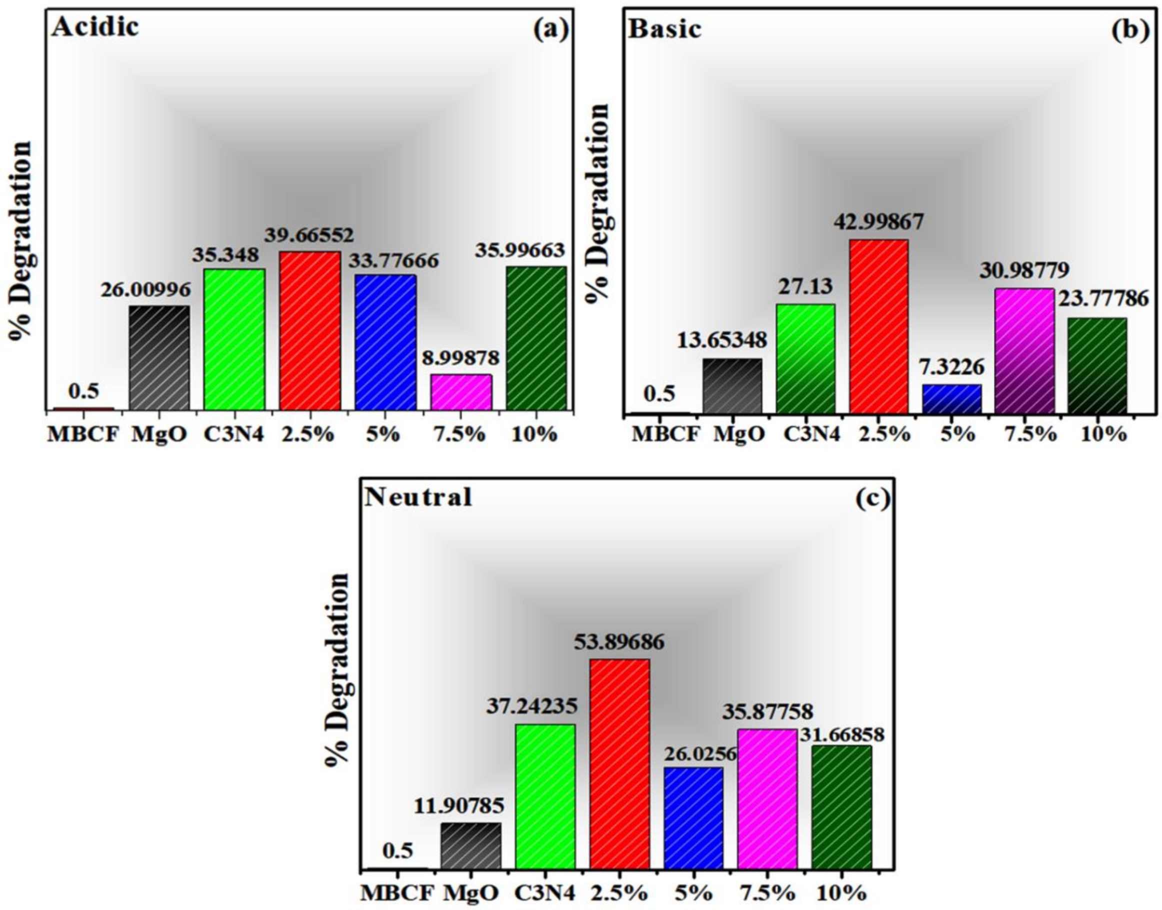

Figure 8: Representing the photocatalytic degradation percentage of samples in acidic, basic and neutral solution of MBCF dye.

The degradation % is minimum for the samples when dye is placed in the dark. Fig. 8 indicated that MBCF dye degradation percentage is maximum (53.89%, 42.99% and 39.66%) for 2.5% Cu-C_3N_4/MgO in neutral, basic and acidic solutions of MBCF dye, respectively. The decrease in degradation on further increasing the doping concentration shows that these nanostructures are the best performing catalyst with 2.5% doping of Cu in C_3N_4/MgO. As described earlier in XRD section, crystallite size decreased with increasing amount of dopants. Addition of Cu (2.5 %) into C_3N_4/MgO showed maximum degradation performance as confirmed by PL results. The 2.5 % sample showed minimum recombination rate which might be owed to the increased amount of defects produced in the lattice after doping [34, 55]. Moreover, the smaller crystallite size reduces the recombination rate and more particles (electrons and holes) are transferred to the surface of catalysts. Cu-doping in C_3N_4/MgO may be due to the balance of trapping carriers causing the longer lifetime of surface charge carriers which results in enhancing PCA [25, 56]. The role of C_3N_4 in fixed amount is very crucial for dye degradation as well. C_3N_4-doped into MgO tend to increase the absorption ability of the sample with an increase in pH and then it starts decreasing [57].

The degradation percentage for the neutral solution of MBCF was maximum, which ascribed to the balancing of hydroxyl groups and holes at the surface. The lower percentage degradation for acidic solution may be due to the fact that dye decomposition takes place at catalyst surface and hydroxyl ions deficiency to react with holes to produce hydroxyl radicals [25]. For basic solution, the degradation percentage of dye decreases, which may be due to the decrease of positive charge at photo-catalyst surface because OH^- ions are absorbed into it [58–60]. A comparison between Cu-C_3N_4/MgO and other famous photocatalysts is provided in the Table 2.

Table 2: Presents the comparison between several famous photocatalysts for the degradation of MB and some other dyes.

Materials	Dyes	Degradation (%)	Time (min)	References
TiO_2	MB	86	120	[61]
V-TiO_2	MB	45	1	[62]
Fe_3O_4/TiO_2/Ag	MB	90	100	[63]
Fe_3O_4@ZnO	MBCF	86	240	[64]

$g\text{-}C_3N_4$	RhB	20	100	[65]
$g\text{-}C_3N_4$ in NaOH	Aqueous Cr^{+}	29.4	120	[66]
$Cu\text{-}C_3N_4/MgO$	MBCF	53	80	Present study

The photo-degradation kinetics by determining the slopes on $\ln\left(\frac{Ct}{Co}\right)$ curves were drawn versus time (Fig. 9) . The rate constants (k) of all samples were determined by pseudo 1^{st} order kinetic equation, $\ln\left(\frac{Co}{Ct}\right) = kt$

.

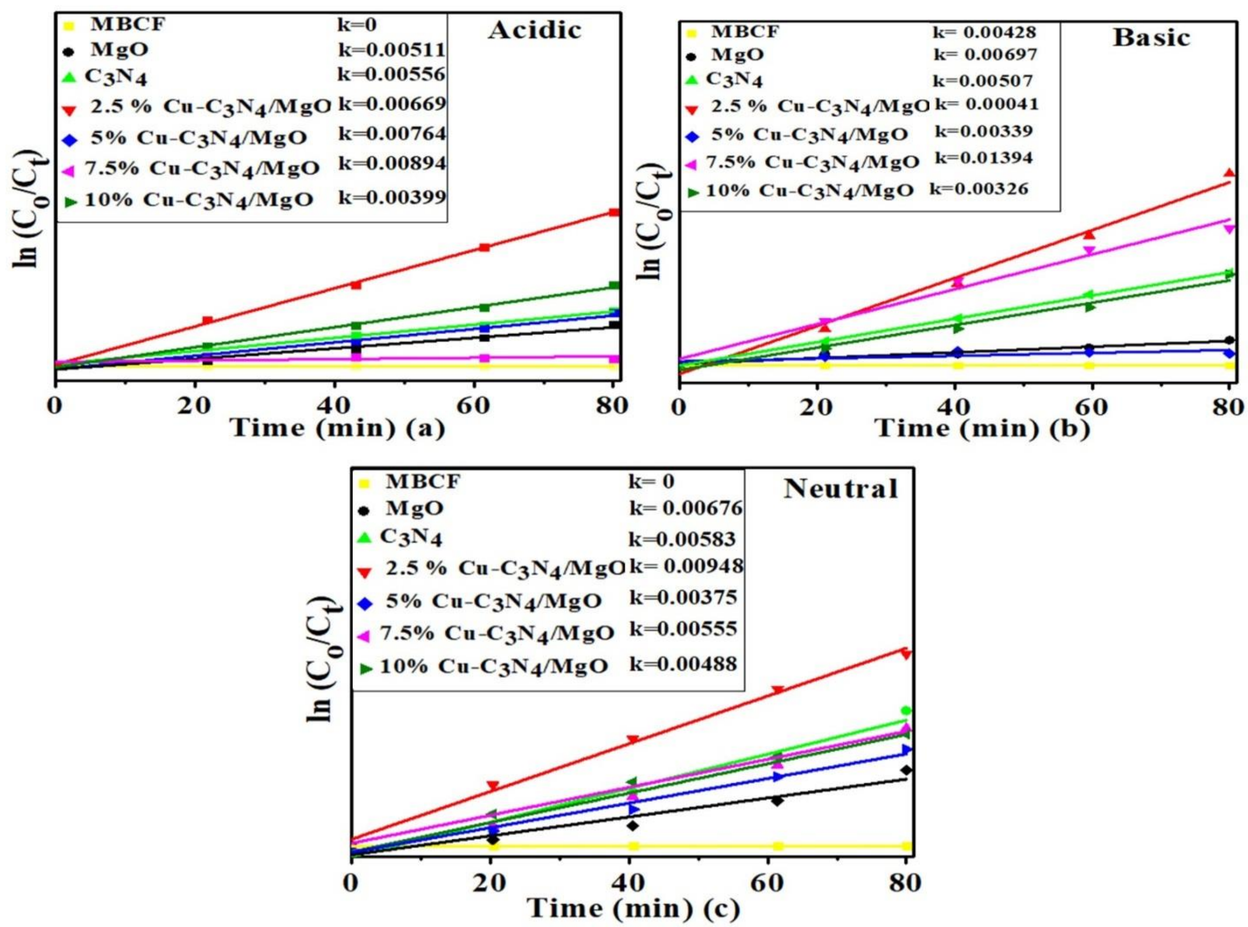

Figure 9: $\ln(C_o/C_t)$ vs time graph of prepared samples at (a) acidic, (b) basic and (c) neutral nature.

Disc diffusion technique was utilized to screen bactericidal sensitivity of prepared nanocomposites. Inhibition zones measured for prepared samples ranged from 1.45 mm to 7.05 mm in diameter against G-negative and positive [Table. 3]. The maximum zone of inhibition observed for 10% Cu-C_3N_4/MgO against *S. aureus* and *E. Coli* were 7.05 mm and 4.15 mm, respectively. Other samples showed comparatively less bactericidal potential which is ascribed to low concentration (0.5 mg/50 µl) as only few NPs are available to cooperate with cell wall. Overall, bactericidal performance of prepared products is better against *S. aureus* at both high and low concentration. Previous studies have reported that bactericidal performance of MgO nanocomposites depends upon the size. This activity increases slowly by decreasing MgO particle size in the range ~ 45-70 nm [67]. This enhanced performance of C_3N_4/MgO with maximum doping of Cu (10%) may be due to incorporation of dopant into matrix which tends to decrease the E_g and crystallite size of the prepared sample. This improved performance can be ascribed to the interaction of microbe cell membranes (having negative charge) and Cu^{2+} and Mg^{+2} ions released by doping with Cu. Released positive ions penetrate the cell casing by reacting with sulfhydryl group inside it. Consequently, strains get damaged enough to lose the growth ability of cells (Fig. 10) [25].

Table 3: Bactericidal action of MgO and Cu-doped C_3N_4/MgO.

Samples	*S. aureus*		*E. coli*	
	Inhibition Zone (mm)		Inhibition Zone (mm)	
	0.5 mg/50 µl	1.0 mg/50 µl	0.5 mg/50 µl	1.0 mg/50 µl
MgO	1.55	2.05	1.45	1.80
C_3N_4	0	0	0	1.60
2.5% Cu-C_3N_4/MgO	2.65	4.40	2.60	3.15
5 % Cu-C_3N_4/MgO	3.45	5.35	3.30	3.40
7.5% Cu-C_3N_4/MgO	3.95	6.45	3.65	3.85
10% Cu-C_3N_4/MgO	4.05	7.05	3.95	4.15

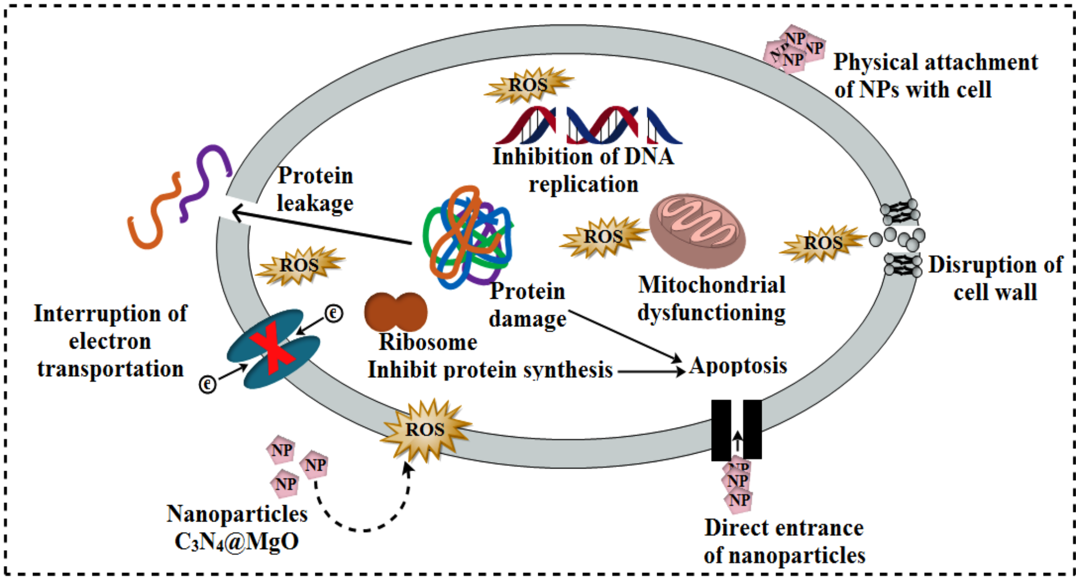

Figure 10: Antimicrobial reaction mechanism of prepared sample.

4. CONCLUSION

Novel Cu-C_3N_4/MgO were prepared through co-precipitation method for dye degradation and antibacterial activities and several properties including structural, morphological and optical were investigated. MgO nanocomposites exhibited FCC cubic structure and transformed itself into nanorods upon Cu and C_3N_4 doping. Doping effects of Cu and C_3N_4 emerged in the form of peak broadening and minor shift to higher angles as shown by XRD results. In FTIR, broad band range of 3040–3550 cm^{-1} indicated the formation of MgO bond while 620- 873 cm^{-1} band was ascribed to MgO bond vibration. UV-Vis spectroscopy demonstrated that MgO showed absorption in region 230-310 nm accompanied by redshift resulting in noteworthy decrease in E_g upon doping of Cu and C_3N_4. PL spectra showed emission at 370 nm with a prominent decrease in intensity upon Cu and C_3N_4 doping. XPS confirmed strong signals of C, N, O, and Cu composition with binding energy modifications of Cu-doped C_3N_4-MgO nanorods. DSC analysis exhibited that the endothermic regions are shifted from 144 $^{\circ}$C towards high temperature range (185°C) upon doping. PCA results revealed that 2.5% Cu-C_3N_4/MgO showed most dye degradation in neutral, basic and acidic mediums. Antibacterial performance investigated by disc diffusion method indicated that maximum dopant 10% Cu-C_3N_4/MgO showed best performance against *S. aureus* and *E. Coli* at both high and low dose concentrations.

ACKNOWLEDGEMENTS

Funding: Authors are thankful to Higher Education Commission, HEC through start research grant project # 21-1669/SRGP/R&D/HEC/2017 Pakistan for financial assistance. Support provided by the Core Research Facilities at the King Fahd University of Petroleum & Minerals, Dhahran, Saudi Arabia is greatly appreciated.

CONFLICT OF INTEREST STATEMENT

This manuscript has no conflict of interest.

REFERENCES

1. Pugazhendhi, A., Prabhu, R., Muruganantham, K., Shanmuganathan, R., Natarajan, S.: Anticancer, antimicrobial and photocatalytic activities of green synthesized magnesium

oxide nanoparticles (MgONPs) using aqueous extract of Sargassum wightii. J. Photochem. Photobiol. B Biol. 190, 86–97 (2019). https://doi.org/10.1016/j.jphotobiol.2018.11.014

2. Rahane, G.K., Jathar, S.B., Rondiya, S.R., Jadhav, Y.A., Barma, S. V., Rokade, A., Cross, R.W., Nasane, M.P., Jadkar, V., Dzade, N.Y., Jadkar, S.R.: Photoelectrochemical Investigation on the Cadmium Sulfide (CdS) Thin Films Prepared using Spin Coating Technique. ES Mater. Manuf. (2020). https://doi.org/10.30919/esmm5f1041

3. Hou, C., Wang, B., Murugadoss, V., Vupputuri, S., Chao, Y., Guo, Z., Wang, C., Du, W.: Recent advances in Co3O4as anode materials for high-performance lithium-ion batteries. Eng. Sci. 11, 19–30 (2020). https://doi.org/10.30919/es8d1128

4. Lv, X., Tang, Y., Tian, Q., Wang, Y., Ding, T.: Ultra-stretchable membrane with high electrical and thermal conductivity via electrospinning and in-situ nanosilver deposition. Compos. Sci. Technol. 200, 108414 (2020). https://doi.org/10.1016/j.compscitech.2020.108414

5. Lu, X., Liu, H., Murugadoss, V., Seok, I., Huang, J., Ryu, J.E., Guo, Z.: Polyethylene glycol/carbon black shape-stable phase change composites for peak load regulating of electric power system and corresponding thermal energy storage. Eng. Sci. 9, 25–34 (2020). https://doi.org/10.30919/es8d901

6. Perl, T.M., Cullen, J.J., Wenzel, R.P., Zimmerman, M.B., Pfaller, M.A., Sheppard, D., Twombley, J., French, P.P., Herwaldt, L.A.: Intranasal Mupirocin to Prevent Postoperative Staphylococcus aureus Infections. N. Engl. J. Med. 346, 1871–1877 (2002). https://doi.org/10.1056/nejmoa003069

7. Bryers, J.D.: Medical biofilms. Biotechnol. Bioeng. 100, 1–18 (2008). https://doi.org/10.1002/bit.21838

8. Aslam, S.: Effect of antibacterials on biofilms. Am. J. Infect. Control. 36, S175.e9-S175.e11 (2008). https://doi.org/10.1016/j.ajic.2008.10.002

9. Nguyen, N.Y.T., Grelling, N., Wetteland, C.L., Rosario, R., Liu, H.: Antimicrobial Activities and Mechanisms of Magnesium Oxide Nanoparticles (nMgO) against Pathogenic Bacteria, Yeasts, and Biofilms. Sci. Rep. 8, 1–23 (2018). https://doi.org/10.1038/s41598-018-34567-5

10. Franke, M.E., Koplin, T.J., Simon, U.: Metal and metal oxide nanoparticles in chemiresistors: Does the nanoscale matter? Small. 2, 36–50 (2006). https://doi.org/10.1002/smll.200500261

11. Wang, S., Wang, Z., Zha, Z.: Metal nanoparticles or metal oxide nanoparticles, an efficient and promising family of novel heterogeneous catalysts in organic synthesis. J. Chem. Soc. Dalt. Trans. 9363–9373 (2009). https://doi.org/10.1039/b913539a

12. Carrara, S., Bavastrello, V., Ricci, D., Stura, E., Nicolini, C.: Improved nanocomposite materials for biosensor applications investigated by electrochemical impedance spectroscopy. Sensors Actuators, B Chem. 109, 221–226 (2005). https://doi.org/10.1016/j.snb.2004.12.053

13. Chertok, B., Moffat, B.A., David, A.E., Yu, F., Bergemann, C., Ross, B.D., Yang, V.C.: Iron oxide nanoparticles as a drug delivery vehicle for MRI monitored magnetic targeting of brain tumors. Biomaterials. 29, 487–496 (2008). https://doi.org/10.1016/j.biomaterials.2007.08.050

14. Jain, A., Wadhawan, S., Kumar, V., Mehta, S.K.: PH-Sensing Strips Based on Biologically Synthesized Ly-MgO Nanoparticles. ACS Omega. 4, 21647–21657 (2019). https://doi.org/10.1021/acsomega.9b01306

15. Luo, X.L., Pei, F., Wang, W., Qian, H. ming, Miao, K.K., Pan, Z., Chen, Y.S., Feng, G.D.: Microwave synthesis of hierarchical porous materials with various structures by controllable desilication and recrystallization. Microporous Mesoporous Mater. 262, 148–153 (2018). https://doi.org/10.1016/j.micromeso.2017.11.037

16. He, Y., Chen, Q., Yang, S., Lu, C., Feng, M., Jiang, Y., Cao, G., Zhang, J., Liu, C.: Micro-crack behavior of carbon fiber reinforced Fe3O4/graphene oxide modified epoxy composites for cryogenic application. Compos. Part A Appl. Sci. Manuf. 108, 12–22 (2018). https://doi.org/10.1016/j.compositesa.2018.02.014

17. Chandane, P., Jadhav, U.: A Simple Colorimetric Detection of Malathion Using Peroxidase Like Activity of Fe3O4 Magnetic Nanoparticles. ES Food Agrofor. (2021). https://doi.org/10.30919/esfaf439

18. Li, D., Sun, J., Ma, R., Wei, J.: High-efficient and Low-cost H2 Production by Solar-driven Photo-thermo-reforming of Methanol with CuO Catalyst. ES Energy Environ. (2020). https://doi.org/10.30919/esee8c722

19. Satpute, S.D., Jagtap, J.S., Bhujbal, P.K., Sonar, S.M., Baviskar, P.K., Jadker, S.R., Pathan, H.M.: Mercurochrome Sensitized ZnO/In2O3 Photoanode for Dye-Sensitized Solar Cell. ES Energy Environ. (2020). https://doi.org/10.30919/esee8c720

20. Mantilaka, M.M.M.G.P.G., De Silva, R.T., Ratnayake, S.P., Amaratunga, G., de Silva, K.M.N.: Photocatalytic activity of electrospun MgO nanofibres: Synthesis, characterization and applications. Mater. Res. Bull. 99, 204–210 (2018). https://doi.org/10.1016/j.materresbull.2017.10.047

21. Wei, J., Zang, Z., Zhang, Y., Wang, M., Du, J., Tang, X.: Enhanced performance of light-controlled conductive switching in hybrid cuprous oxide/reduced graphene oxide

(Cu_2O/rGO) nanocomposites. Opt. Lett. 42, 911 (2017). https://doi.org/10.1364/ol.42.000911

22. Devaraja, P.B., Avadhani, D.N., Nagabhushana, H., Prashantha, S.C., Sharma, S.C., Nagabhushana, B.M., Nagaswarupa, H.P., Prasad, B.D.: Luminescence properties of MgO: Fe 3+ nanopowders for WLEDs under NUV excitation prepared via propellant combustion rout e. J. Radiat. Res. Appl. Sci. 8, 362–373 (2015). https://doi.org/10.1016/j.jrras.2015.02.001

23. Devadathan, D.: SYNTHESIS, CHARACTERIZATION AND PHOTOCATALYTIC ACTIVITY OF MgO NANOPARTICLES.

24. Maji, J., Pandey, S., Basu, S.: Synthesis and evaluation of antibacterial properties of magnesium oxide nanoparticles. Bull. Mater. Sci. 43, 25 (2020). https://doi.org/10.1007/s12034-019-1963-5

25. Rajendran, V., Deepa, B., Mekala, R.: Studies on structural, morphological, optical and antibacterial activity of Pure and Cu-doped MgO nanoparticles synthesized by co-precipitation method. In: Materials Today: Proceedings. pp. 8796–8803. Elsevier Ltd (2018)

26. Bertinetti, L., Drouet, C., Combes, C., Rey, C., Tampieri, A., Coluccia, S., Martra, G.: Surface characteristics of nanocrystalline apatites: Effect of Mg surface enrichment on morphology, surface hydration species, and cationic environments. Langmuir. 25, 5647–5654 (2009). https://doi.org/10.1021/la804230j

27. Zhao, Z., Dai, H., Du, Y., Deng, J., Zhang, L., Shi, F.: Solvo- or hydrothermal fabrication and excellent carbon dioxide adsorption behaviors of magnesium oxides with multiple morphologies and porous structures. Mater. Chem. Phys. 128, 348–356 (2011).

https://doi.org/10.1016/j.matchemphys.2011.02.073

28. Camtakan, Z., Erenturk, S.A., Yusan, S.D.: Magnesium oxide nanoparticles: Preparation, characterization, and uranium sorption properties. Environ. Prog. Sustain. Energy. 31, 536–543 (2012). https://doi.org/10.1002/ep.10575

29. Veldurthi, S., Shin, C.H., Joo, O.S., Jung, K.D.: Synthesis of mesoporous MgO single crystals without templates. Microporous Mesoporous Mater. 152, 31–36 (2012). https://doi.org/10.1016/j.micromeso.2011.11.044

30. Gillet, E., Ealet, B.: Characterization of sapphire surfaces by electron energy-loss spectroscopy. Surf. Sci. 273, 427–436 (1992). https://doi.org/10.1016/0039-6028(92)90079-L

31. Rodriguez, J.A., Jirsak, T., Chaturvedi, S.: Reaction of H2S with MgO(100) and Cu/MgO(100) surfaces: Band-gap size and chemical reactivity. J. Chem. Phys. 111, 8077–8087 (1999). https://doi.org/10.1063/1.480141

32. Nor Fadilah, C., Norlida, K., Nurhanna, B., Kelimah, E.: Effect of cu doped in mgo on nanostructures and their band gap energies. Solid State Phenom. 290 SSP, 323–328 (2019). https://doi.org/10.4028/www.scientific.net/SSP.290.323

33. Kumari, L., Li, W.Z., Vannoy, C.H., Leblanc, R.M., Wang, D.Z.: Synthesis, characterization and optical properties of Mg(OH)2 micro-/nanostructure and its conversion to MgO. Ceram. Int. 35, 3355–3364 (2009). https://doi.org/10.1016/j.ceramint.2009.05.035

34. Mageshwari, K., Mali, S.S., Sathyamoorthy, R., Patil, P.S.: Template-free synthesis of MgO nanoparticles for effective photocatalytic applications. Powder Technol. 249, 456–462 (2013). https://doi.org/10.1016/j.powtec.2013.09.016

35. (5) (PDF) Advances in catalytic/photocatalytic bacterial inactivation by nano Ag and Cu coated surfaces and medical devices, https://www.researchgate.net/publication/326260972_Advances_in_catalyticphotocatalytic_bacterial_inactivation_by_nano_Ag_and_Cu_coated_surfaces_and_medical_devices
36. Rtimi, S., Pulgarin, C., Bensimon, M., Kiwi, J.: Colloids and Surfaces B : Biointerfaces New evidence for Cu-decorated binary-oxides mediating bacterial inactivation / mineralization in aerobic media. Colloids Surfaces B Biointerfaces. 144, 222–228 (2016). https://doi.org/10.1016/j.colsurfb.2016.03.072
37. Manuscript, A.: Nanoscale Biological Applications : A Review. (2019). https://doi.org/10.1039/C9NR04568F
38. Prince, M.J..: Optical Analysis of Cu Doped Mg Nanoparticles Using Co-Precipitation Method. Int. J. Res. Appl. Sci. Eng. Technol. V, 1775–1792 (2017). https://doi.org/10.22214/ijraset.2017.10261
39. Yousefi, S., Ghasemi, B., Tajally, M., Asghari, A.: Optical properties of MgO and Mg(OH)2 nanostructures synthesized by a chemical precipitation method using impure brine. J. Alloys Compd. (2017). https://doi.org/10.1016/j.jallcom.2017.04.036
40. Balakrishnan, G., Velavan, R., Mujasam Batoo, K., Raslan, E.H.: Microstructure, optical and photocatalytic properties of MgO nanoparticles. Results Phys. 16, 14–17 (2020). https://doi.org/10.1016/j.rinp.2020.103013
41. Anticancer, antimicrobial and photocatalytic activities of green synthesized magnesium oxide nanoparticles (MgONPs) using aqueous extract of Sargassum wightii - ScienceDirect, https://www.sciencedirect.com/science/article/pii/S1011134418312090
42. Paradiso, D., Larese, J.Z.: Solvent Free Deposition of Cu on Nanocubes of MgO. J. Phys.

Chem. C. 124, 14564–14572 (2020). https://doi.org/10.1021/acs.jpcc.0c01790

43. Devaraja, P.B., Nagabhushana, H., Sharma, S.C., Naik, R., Prashantha, S.C., Nagaswarupa, H.P., Anantharaju, K.S., Premkumar, H.B., Jnaneshwara, D.M.: Spectroscopic and photoluminescence properties of MgO:Cr3+ nanosheets for WLEDs. Displays. 41, 16–24 (2016). https://doi.org/10.1016/j.displa.2015.10.006

44. Selvakumar, N., Vettivel, S.C.: Thermal, electrical and wear behavior of sintered Cu-W nanocomposite. Mater. Des. 46, 16–25 (2013). https://doi.org/10.1016/j.matdes.2012.09.055

45. Nejati, K., Rezvani, Z., Massoumi, B.: Syntheses and investigation of thermal properties of copper complexes with azo-containing Schiff-base dyes. Dye. Pigment. 75, 653–657 (2007). https://doi.org/10.1016/j.dyepig.2006.07.019

46. Zein based magnesium oxide nanowires: Effect of anionic charge on size, release and stability — Augusta University Research Profiles, https://augusta.pure.elsevier.com/en/publications/zein-based-magnesium-oxide-nanowires-effect-of-anionic-charge-on-

47. Hou, C., Yang, W., Xie, X., Sun, X., Wang, J., Naik, N., Pan, D., Mai, X., Guo, Z., Dang, F., Du, W.: Agaric-like anodes of porous carbon decorated with MoO2 nanoparticles for stable ultralong cycling lifespan and high-rate lithium/sodium storage. J. Colloid Interface Sci. 596, 396–407 (2021). https://doi.org/10.1016/j.jcis.2021.03.149

48. Shao, Y., Wang, J., Engelhard, M., Wang, C., Lin, Y.: Facile and controllable electrochemical reduction of graphene oxide and its applications. J. Mater. Chem. 20, 743–748 (2010). https://doi.org/10.1039/b917975e

49. Zhang, J., Zhang, M., Zhang, G., Wang, X.: S doped g-C3N4(. 2012, 2, 940−948).pdf.

(2012)

50. Poulston, S., Parlett, P.M., Stone, P., Bowker, M.: Surface oxidation and reduction of CuO and Cu2O studied using XPS and XAES. Surf. Interface Anal. 24, 811–820 (1996). https://doi.org/10.1002/(SICI)1096-9918(199611)24:12<811::AID-SIA191>3.0.CO;2-Z

51. Standley K: Electrical Properties of Ferrites and Garnets. Oxide Magnetic Materials, Second Edition. Clarendon Press Oxford (1972)

52. Lam, S.M., Sin, J.C., Abdullah, A.Z., Mohamed, A.R.: Degradation of wastewaters containing organic dyes photocatalysed by zinc oxide: A review. Desalin. Water Treat. 41, 131–169 (2012). https://doi.org/10.1080/19443994.2012.664698

53. Taurian, O.E., Springborg, M., Christensent, N.E., Technical, T.: (Received 20 December 1984 by M. Cardona). Quantum. 55, 351–355 (1985)

54. (PDF) Catalytic Photodegradation of Methyl orange using MgO nanoparticles prepared by molten salt method, https://www.researchgate.net/publication/286912608_Catalytic_Photodegradation_of_Methyl_orange_using_MgO_nanoparticles_prepared_by_molten_salt_method

55. Kakade, P.M., Kachere, A.R., Mandlik, N.T., Rondiya, S.R., Jadkar, S.R., Bhosale, S. V.: Graphene Oxide Assisted Synthesis of Magnesium Oxide Nanorods. ES Mater. Manuf. (2020). https://doi.org/10.30919/esmm5f1044

56. Zhang, Q., Dai, J., Liao, M., Duan, T., Yao, W.: Doughnut-structured FeS2@C nanorings: Towards the efficient synthesis and application in high-performance Li-ion cathode. Eng. Sci. 7, 43–51 (2019). https://doi.org/10.30919/es8d689

57. Zhou, J., Ji, X., Zhou, X., Guo, J., Sun, J., Liu, Y.: Three-dimensional g-C3N4/MgO composites as a high-performance adsorbent for removal of Pb(II) from aqueous solution.

Sep. Sci. Technol. 54, 2817–2829 (2019). https://doi.org/10.1080/01496395.2018.1553983

58. Kazeminezhad, I., Sadollahkhani, • Azar: Influence of pH on the photocatalytic activity of ZnO nanoparticles. https://doi.org/10.1007/s10854-016-4284-0

59. Miao, K. kang, Luo, X. lin, Wang, W., Guo, J. le, Guo, S. fan, Cao, F. jiu, Hu, Y. qiao, Chang, P. mei, Feng, G. dong: One-step synthesis of Cu–SBA-15 under neutral condition and its oxidation catalytic performance. Microporous Mesoporous Mater. 289, 109640 (2019). https://doi.org/10.1016/j.micromeso.2019.109640

60. Cai, J., Xu, W., Liu, Y., Zhu, Z., Liu, G., Ding, W., Wang, G., Wang, H., Luo, Y.: Robust construction of flexible bacterial cellulose@Ni(OH)2 paper: Toward high capacitance and sensitive H2O2 detection. Eng. Sci. 5, 21–29 (2019). https://doi.org/10.30919/es8d666

61. Arbuj, S.S., Hawaldar, R.R., Mulik, U.P., Wani, B.N., Amalnerkar, D.P., Waghmode, S.B.: Preparation, characterization and photocatalytic activity of TiO2 towards methylene blue degradation. Mater. Sci. Eng. B Solid-State Mater. Adv. Technol. 168, 90–94 (2010). https://doi.org/10.1016/j.mseb.2009.11.010

62. Bettinelli, M., Dallacasa, V., Falcomer, D., Fornasiero, P., Gombac, V., Montini, T., Romanò, L., Speghini, A.: Photocatalytic activity of TiO2 doped with boron and vanadium. J. Hazard. Mater. 146, 529–534 (2007). https://doi.org/10.1016/j.jhazmat.2007.04.053

63. Zhang, L., Wu, Z., Chen, L., Zhang, L., Li, X., Xu, H., Wang, H., Zhu, G.: Preparation of magnetic Fe3O4/TiO2/Ag composite microspheres with enhanced photocatalytic activity. Solid State Sci. 52, 42–48 (2016). https://doi.org/10.1016/j.solidstatesciences.2015.12.006

64. Winatapura, D.S., Dewi, S.H., Adi, W.A.: Synthesis, characterization, and photocatalytic

activity of Fe3O4@ZnO nanocomposite. Int. J. Technol. 7, 408–416 (2016). https://doi.org/10.14716/ijtech.v7i3.2952

65. Qi, K., Li, Y., Xie, Y., Liu, S.Y., Zheng, K., Chen, Z., Wang, R.: Ag loading enhanced photocatalytic activity of g-C 3 N 4 porous nanosheets for decomposition of organic pollutants. Front. Chem. 7, (2019). https://doi.org/10.3389/fchem.2019.00091

66. Zhang, Q., Liu, S., Zhang, Y., Zhu, A., Li, J., Du, X.: Enhancement of the photocatalytic activity of g-C3N4 via treatment in dilute NaOH aqueous solution. Mater. Lett. 171, 79–82 (2016). https://doi.org/10.1016/j.matlet.2016.02.043

67. Lei, H., Dianqing, L.I., Yanjun, L.I.N., Evans, D.G., Xue, D.: Influence of nano-MgO particle size on bactericidal action against Bacillus subtilis var . niger. 50, 514–519 (2005). https://doi.org/10.1360/04wb0075

Click here to access/download
Supplementary Material
Supplementary File.docx